Hindawi
Geofluids
Volume 2018, Article ID 2416481, 11 pages
https://doi.org/10.1155/2018/2416481

*Research Article*

# Shear-induced Permeability Evolution of Sandstone Fractures

**Hongwei Zhang**,[1] **Zhijun Wan**,[1] **Zijun Feng**,[2] **and Jinwen Wu**[3]

[1]*Key Laboratory of Deep Coal Resource Mining (CUMT), Ministry of Education of China, School of Mines, China University of Mining & Technology, Xuzhou 221116, China*
[2]*Department of Mining Engineering, Taiyuan University of Technology, Taiyuan, Shanxi 030024, China*
[3]*School of Science, North University of China, Taiyuan, Shanxi 030051, China*

Correspondence should be addressed to Zhijun Wan; zhjwan@cumt.edu.cn

Received 4 July 2018; Revised 5 October 2018; Accepted 18 October 2018; Published 23 December 2018

Guest Editor: Wen Wang



In underground coal mines, shear-induced changes in regional fluid flow are a major factor causing water inrushes from faults into working faces. Shear slip along preexisting fractures tends to be activated during hydraulic fracturing, and this movement can either enhance or diminish hydraulic fracturing efficiency. To prevent water inrush disasters and further hydraulic fracturing, understanding the evolution of shear-induced permeability in fractures in sedimentary rock is very important. In this study, the evolution of shear-induced permeability in saw-cut sandstone fractures with three different types of surface roughness was investigated by conducting triaxial shear tests and examining the 3-D topography of the unsheared and sheared fracture surfaces. The results allow several important conclusions to be drawn. (1) The permeability of fractures follows a three-stage shear-displacement-dependent evolution. The permeability remains unchanged in the first stable stage. After that, permeability decreases sharply with increasing shear displacement. Finally, the permeability enters a second stable stage. (2) The shear stress versus shear-displacement curves can also be divided into three stages, namely, a stress adjustment stage, a stage of increasing stress, and a stable stage. During the experiments, the fractures always experienced stick-slip shear in the stable stage. The oscillations of the shear stress in the stick-slip stage had a higher frequency for fractures with rougher surfaces. In addition, the rougher surfaces exhibited a greater permeability drop after shearing than that shown by smoother fracture surfaces. (3) The 3-D scanning results imply that the coupled effects of grinding (plus scraping) and sealing lead to decreased permeability. During shearing, the fracture walls grind and scrape against each other resulting in partial flattening of the fracture surface and the production of fault gouge in the fracture. This leads in turn to the flow pathways being partially sealed by crushed mineral grains.

## 1. Introduction

During underground coal mining, mining-triggered shear failure of roof strata, hydraulic fracturing-induced shear slip of preexisting fractures, and fault slip-activated groundwater inrushes can occur if the preexisting hydraulic and mechanical equilibrium conditions are disrupted [1–6]. Faults in sedimentary rocks that are dominated by deformation bands tend to act as barriers to fluid flow, and these faults compartmentalize fluids, whereas faults characterized by discrete fractures act as fluid pathways [7–12]. In sedimentary formations, shear slip of fractured rock associated with dilation or compaction can significantly change fracture permeability, thus affecting fluid flow [13–15]. Enhanced fluid flows may be beneficial for desorbing of coal seam gas and increasing geothermal energy extraction [16–21], but this enhanced flow will be disadvantageous for groundwater protection and mining [22]. Therefore, to achieve safe and efficient mining in coal seams, knowledge of the evolution of fracture permeability with shearing is very important.

Rock fractures tend to remain stable under equilibrium hydraulic and mechanical conditions. When stresses are redistributed by mining or excavation, deformation events like strata movement or rock failure can be triggered. This deformation can greatly influence the permeability of

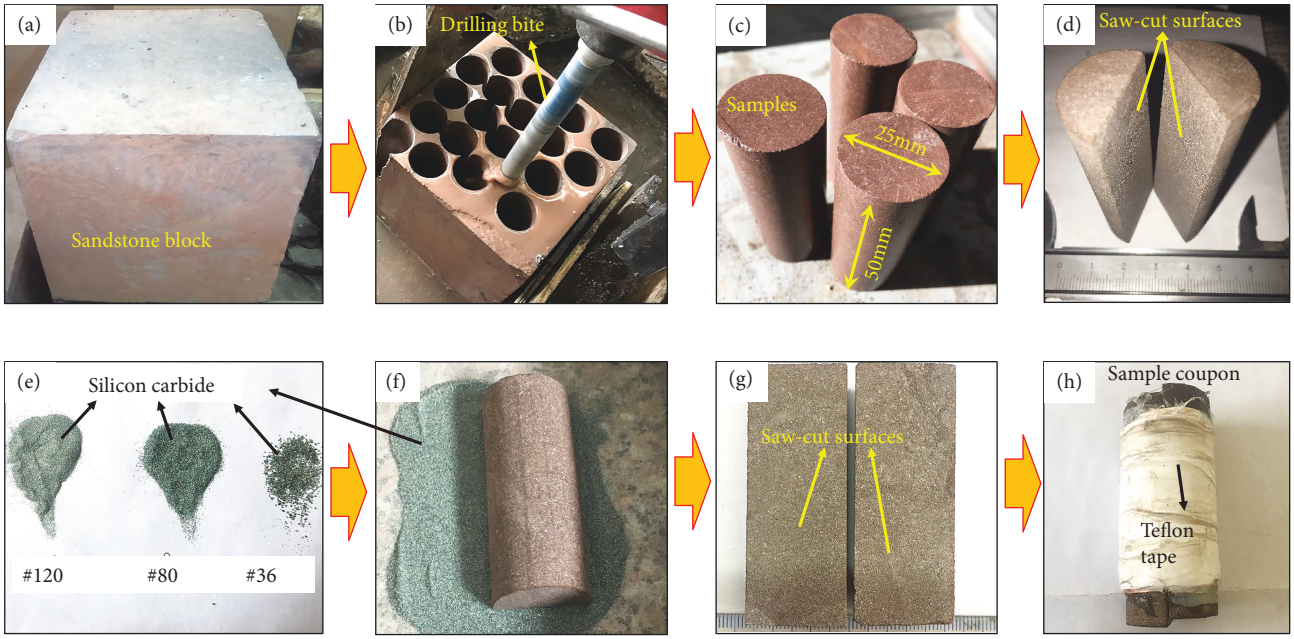


Figure 1: Sample preparation: (a) sandstone block; (b) coring; (c) cylinders with the diameter of 25 mm and the height of 50 mm; (d) halved semicylindrical samples; (e) #120 Grit, #80 Grit, and #36 Grit (a lower value implies a coarser silicon carbide powder, thus implying a rougher surface); (f) grinding the planar surfaces by silicon carbide powder; (g) ground surfaces; (h) combining the specimen by Teflon tape.

fractures. The spatial variability of fault and fracture permeability is complex [23]. The mechanisms of shear-induced permeability evolution differ because of the complexity of rock discontinuities and the anisotropy of rocks.

The permeability of fractured rock masses is stress dependent [24]. In general, the evolution of shear-induced permeability is affected by several factors including the stress state, fracture geometry, porosity evolution, and the effects of cementation and grain size reduction. Shear-induced permeability reduction can also be caused by shear-enhanced compaction [25].

Fracture geometry is also an important factor in the dilation or compression of fracture apertures during shearing [26–28]. Rougher fractures with greater surface topography commonly undergo slip opening due to mismatched surfaces. This mismatch results in increased fracture apertures (or opening). For smoother fracture surfaces, dilation may be changed to compression resulting in a permeability decrease.

Part of the shear-induced permeability evolution of fractures is related to the development or destruction of porosity, for example, porosity increase due to dilation or dissolution/scraping [29–31]. Porosity can be reduced by the formation of gouge or chemical compaction and chemical precipitation [32, 33]. Permeability can be enhanced because of shear dilation, but it can also be reduced by the formation of gouge [33–38]. In addition, fractures acting as fluid pathways may become impermeable during deformation if they become partially cemented; this will limit the amount of fluid that can pass through the fracture [39]. That is to say, the permeability of fractures may decrease during deformation because the gouge or cement produced during slip can block fluid flow [40].

Grain size is an important factor, and in some cases, it is the determining factor for fracture permeability. This is particularly true for clay-rich samples. Experimental studies have found that coarse-grained gouge is the most permeable and that gouge permeability decreases after shearing. Conversely, fine-grained gouge in most cases has a lower permeability, but its permeability does not change significantly after shearing [41]. Thus, it appears that coarse grains or rough surfaces can be transformed into fine grains and a smooth surface, during shearing, and this can cause permeability to decrease. There are also other mechanisms that contribute to the long-term sealing and healing effect of fractures and faults after shearing [42, 43].

In this study, we focused on investigating the evolution of shear-induced permeability in saw-cut fractures in sandstone and on the basic mechanisms leading to permeability changes. To this end, we conducted triaxial shear and water injection tests and analyzed the fracture surfaces before and after shearing. This paper is organized as follows. The first sections describe the sample preparation, the shearing test, and the fracture surface analysis method. Next, the test results are described and their bearing on coupled shear and fracture permeability discussed. In addition, the results of profile tests are presented and used to discuss the mechanisms of permeability changes during shearing. Finally, several important conclusions are drawn.

## 2. Materials and Methodology

*2.1. Sample Preparation.* Sandstone was used to conduct the shear-permeability tests. Sandstone blocks (Figure 1(a)) were collected from an open pit mine. The blocks were carefully selected to exclude fractures, discontinuities, and

Table 1: Physical and mechanical properties of sandstone.

| | Uniaxial compression strength | Elastic modulus | Tensile strength | Density |
|---|---|---|---|---|
| Physicomechanical properties | 64.0 MPa | 9.8 MPa | 3.4 MPa | 2650 kg/m$^3$ |

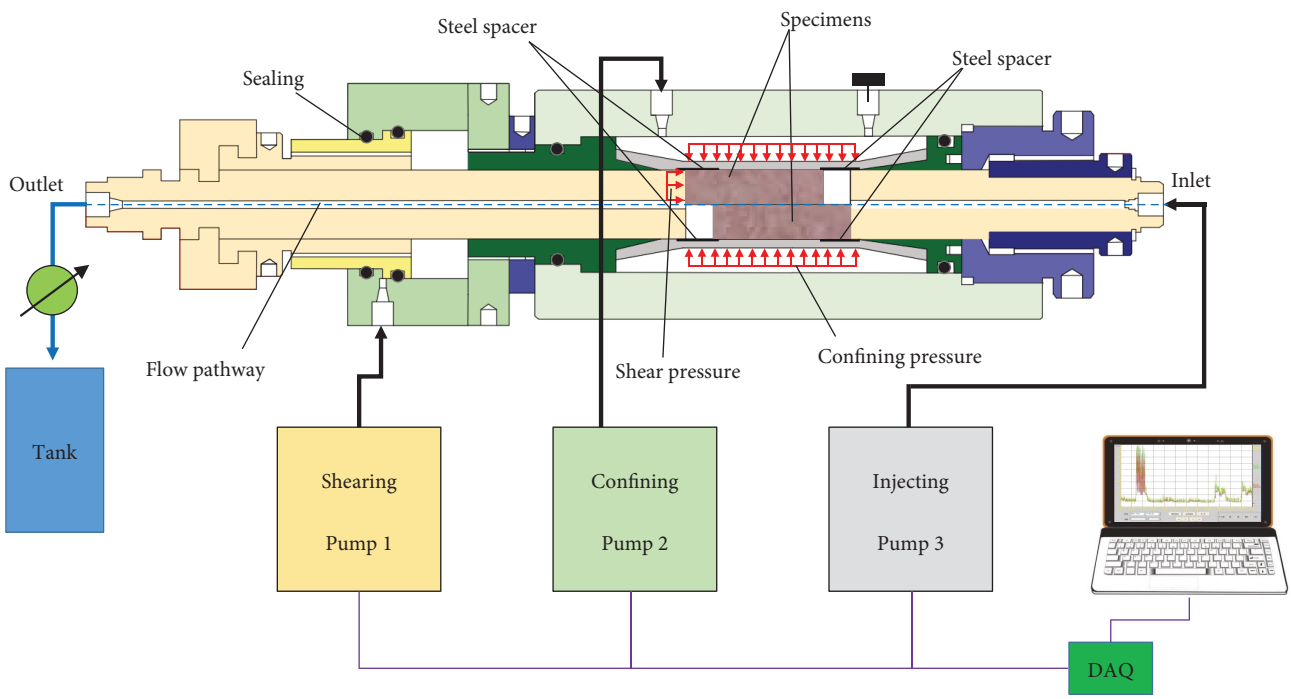


Figure 2: Shear-permeability test apparatus.

microcracks in the blocks that could influence the test results. The blocks were cut into cylinders with a diameter of 25 mm and height of 50 mm (Figures 1(b) and 1(c)). Both ends of the cylindrical samples were ground to ensure uniform end conditions. The physical and mechanical properties of sandstone are shown in Table 1.

To achieve the shear test of fractures, each sandstone sample was cut in half longitudinally with a rock saw to form two half cylinders (Figure 1(d)). The cut surfaces were ground to remove surface irregularities that might influence the test results. This was done using different grain size grinding powders, namely, #36, #80, and #120 grit silicon carbide (Figures 1(e), 1(f), and 1(g)). It should be noted that lower value implies coarser powder. The fracture surfaces ground with the #36, #80, and #120 grit powders were called #36 Grit, #80 Grit, and #120 Grit surfaces, respectively. The ground half cylinder blocks were joined to make the shear-permeability test specimen. To allow for slip displacement during shearing, the blocks were offset from one another with an initial offset of 10 mm. The blocks were held together with Teflon tape (Figure 1(h)).

*2.2. Shear-Permeability Testing Apparatus and Test Procedures.* The shear-permeability tests were performed using a triaxial test system (Figure 2). This system consists of three main parts: pumps, the triaxial compression press, and monitoring equipment. The triaxial compression press has three servocontrolled pumps. The press has a maximum pressure capacity of 70.0 MPa, and the pumps can provide a maximum flow rate of 100 ml/min. The minimum flow rate of each pump is 0.01 ml/min, and the display resolution of the pressure transducer (an Omega PX409) is $1 \times 10^{-3}$ Pa. The pumps can be controlled to provide a constant pressure or a constant flow rate. The triaxial pressure cell was used to shear the specimens along the saw-cut fracture under a confining pressure. However, the shearing test could not be conducted in an unmodified triaxial cell because the offset ends of the specimens (Figure 1(h)) could not be sealed. Therefore, two steel ring spacers were used to protect the latex membrane in the triaxial cell and to ensure that the specimen was sheared. It should be noted that although the specimens were wrapped with Teflon tape, friction between the triaxial cell's confining latex membrane and specimen surface could not be entirely eliminated but it was minimized to some extent by the Teflon tape. Therefore, the stress recorded for the pressure platens on the triaxial press was no doubt somewhat higher than the shear stress experienced by the fracture. This was an unavoidable experimental limitation.

The shearing tests were conducted by following these steps: (1) place a specimen in the center of the triaxial cell,

(2) apply a servocontrolled confining pressure of 3.0 MPa with the confining pressure pump, (3) provide a constant injection pressure of 0.25 MPa from the injection pump, (4) shear the sample with a constant shear velocity of 10 $\mu$m/s with pressure from the shearing pump, and (5) record the pressure and flow rates during shearing. Three sandstone specimens, each with a different surface roughness, were tested using this procedure. All the experiments were performed at room temperature (~20°C).

*2.3. Surface Roughness Measurement.* Three-dimensional reconstructions of the saw-cut-simulated fracture surfaces were created both before and after shearing using a non-contact confocal profilometer. The profilometer consists of a nanomodule, a demodulator, and related software. The profilometer can collect 3-D data from an area with a maximum dimension of 10 mm × 10 mm. A 0.1 $\mu$m measurement step was used to scan the sample surfaces. The scan velocity and acquisition rate were set at 20 mm/s and 1000 Hz, respectively. The 3-D reconstructions were analyzed using the software provided by the profilometer's manufacturer. The tested parameters (root mean square height, skewness, kurtosis, maximum peak height, maximum pit height, maximum height, and arithmetic mean height) were calculated according to International Organization for Standardization (ISO) 25178 [44].

The 3-D reconstructions of unsheared and sheared surfaces were created by placing the specimens on the profilometer platform, selecting the area for scanning, setting the scanning parameters, and then automatically scanning the selected area using the profilomtere's software. The three specimens were scanned before and after shearing.

## 3. Permeability of Fractures: Theoretical Backgrounds

The cubic law, assuming that the fracture consists of the region bounded by two perfectly smooth parallel plates separated from each other by a constant distance, has traditionally been employed to describe the fluid flow through rock fractures (Figure 3). According to this model, the permeability in the fracture is defined as [45]

$$k_f = \frac{b^2}{12}, \tag{1}$$

where $k_f$ (m$^2$) is the permeability of the fracture with an aperture of $b$ (m).

If the flow is steady and isothermal, the relationship between the flow rate and pressure drop in a fracture can be developed from Darcy's law and expressed as

$$Q = -\frac{k_f A \Delta P}{\mu l}, \tag{2}$$

where $Q$ (m$^3$/s) and $\Delta P$ (Pa) are the flow rate and pressure drop, respectively. The fracture parameters $A$ (m$^2$) and $l$ (m) denote the cross-sectional flow area and fracture length, respectively. $A = bw$ and $w$ (m) is the fracture width. $\mu$ (Pa·s) is the viscosity of fluid which is $1.005 \times 10^{-3}$ Pa · s for water at 20°C.

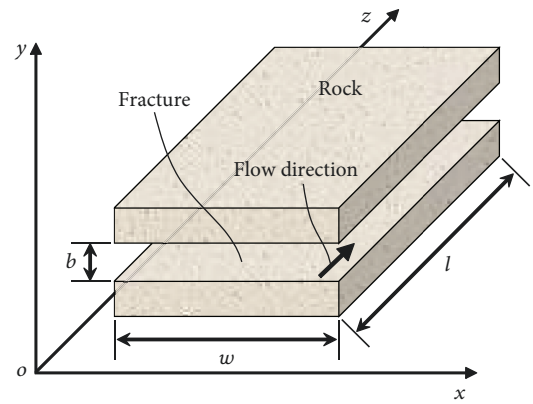


Figure 3: Scheme of flow between parallel plates.

By combining equations (1) and (2), we can derive the basic equation describing the permeability of a fracture with an aperture of $b$. It should be noted that the sample length $l$ increases with shearing time $t$ during the shear process. Therefore, the permeability can be expressed as

$$k_f = \left(-\frac{\sqrt{3}Q\mu(l_0 + v_t t)}{6w\Delta P}\right)^{2/3}, \tag{3}$$

where $v_t$ (m/s) is the shearing velocity.

## 4. Results and Discussion

*4.1. Evolution of Shear-Induced Permeability in Sandstone Fractures.* Figure 4 presents the shear-permeability evolution of sandstone fractures for the three different types of surface roughness studied, the #36 Grit, #80 Grit, and #120 Grit surfaces. The graphs on the left in Figure 4 show the shear stresses and permeability values in the fractures during the entire experiment; the graphs on the right show stages of stable shear and permeability changes magnified from the graphs on the left. In these figures, the black lines represent shear versus displacement and the red lines show permeability versus displacement.

*4.1.1. Shear Behavior.* The shear stress-displacement curves for the saw-cut fractures can be divided into three stages: (1) a stress adjustment stage, (2) a stage showing increasing stress, and (3) a stable shear stage. During the stress adjustment stage, the shear-displacement curve's convexity is downward; this stage persists from 0 mm to about 1 mm displacement. During the increasing stress stage, the shear stress rises with increasing shear displacement. This stage ends when peak shear strength is reached, and the stage is followed by the stable shear stage.

It is generally acknowledged that a fracture's surface roughness increases its shear resistance. Hence, the peak shear strength for a fracture in rock should be greater for a

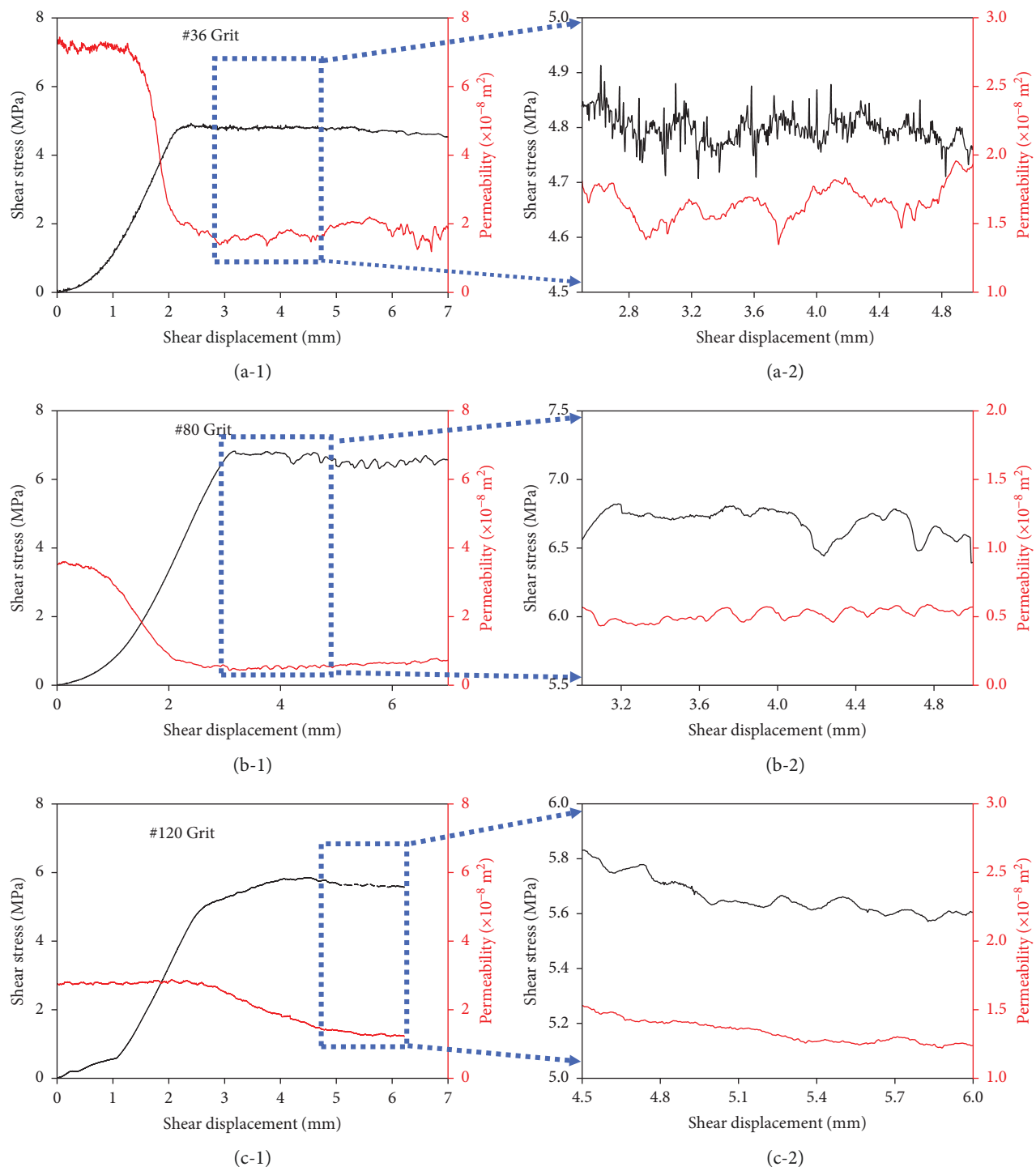


Figure 4: Shear-induced permeability evolution of sandstone fractures: (a-1) shear response and permeability evolution of #36 Grit fracture; (a-2) shear response and permeability evolution of #36 Grit fracture during stable shear stage; (b-1) shear response and permeability evolution of #80 Grit fracture; (b-2) shear response and permeability evolution of #80 Grit fracture during stable shear stage; (c-1) shear response and permeability evolution of #120 Grit fracture; (c-2) shear response and permeability evolution of #120 Grit fracture during stable shear stage.

fracture with a rougher surface. As mentioned in the methodology section, Section 2.2, the shear stress imposed by the triaxial press on the pressure cell during the tests was higher than the actual shear stress experienced by the fractures in the specimens because of the friction between the confining latex membrane and the sample surface. However, we believe that the shapes of the curves reflect the actual failure response of the fractures.

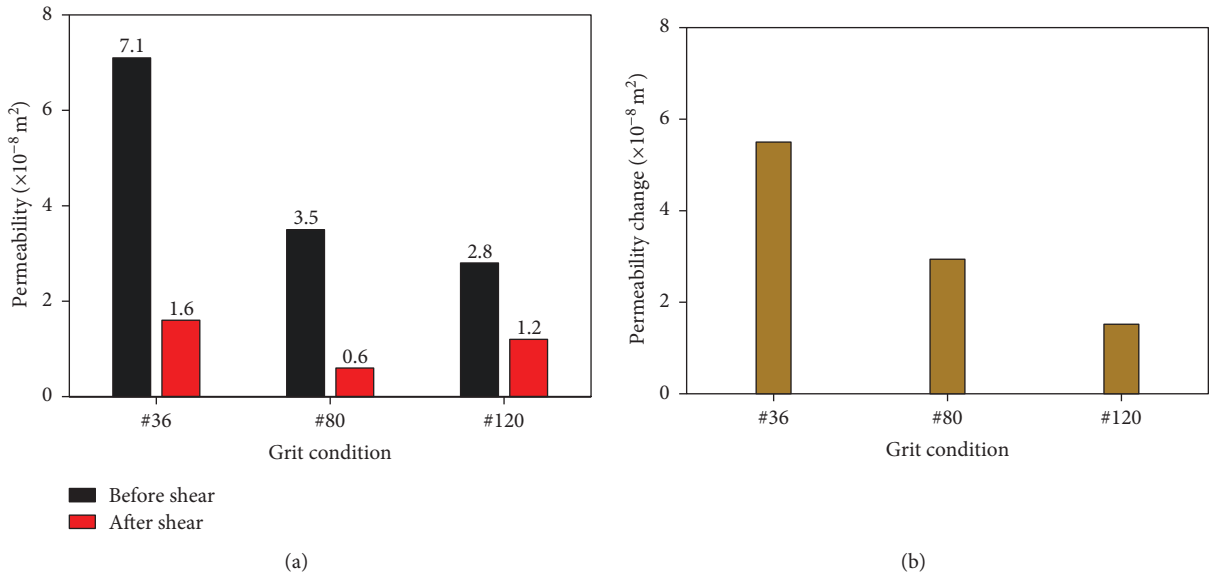


Figure 5: Permeability values of sandstone fractures before and after shearing tests: (a) permeability values before and after shearing; (b) permeability drops of sandstone fractures.

The most important factor affecting a fracture's shear behavior is the size and condition of the contact area between the fracture walls. Contact areas can possess different types of roughness and apertures and be subjected to different normal effective stresses [46]. For these experiments using modified saw-cut-simulated fractures under a constant effective stress, the evolution of the fracture aperture is mainly controlled by the fracture surface roughness. That is, the changes in shear stress during the stable shear stage should depend only on the roughness of the fracture. As can be seen from the graphs on the right side of Figure 4, the shear-displacement curves become smoother as the roughness of the fracture surface decreases. After the shear stress peaks, the shear stress oscillates with a high frequency for the fracture roughened with #36 grit. This is unstable stick-slip behavior [47], and shearing probably decreases fracture surface roughness, reduces grain sizes, and rotates crushed grains. For the fracture roughened with #80 grit, the shear stress oscillates at a much lower frequency, and the fracture ground with #120 grit is even more stable. This progression indicates that stick-slip behavior diminishes as surface roughness decreases. Shearing a rougher surface results in greater shear stress oscillations.

*4.1.2. Permeability Evolution.* The evolution of shear-induced permeability in fractures is related to changes in porosity and grain size. In Figure 4, the red lines show the evolution of shear-induced permeability. The permeability curves can be divided into three stages: (1) a stable stage, (2) a stage of decreasing permeability, and (3) a second stable stage.

In the first stable permeability stages that are shown in Figures 4(a-1), 4(b-1), and 4(c-1), although the shear stresses increase, the permeability values remain fairly constant. This suggests that the initial stress adjustments do not affect the aperture of the fracture significantly. The permeability values at the beginning of the first stable stages (at 0 mm displacement) are $7.1 \times 10^{-8}$ m$^2$, $3.5 \times 10^{-8}$ m$^2$, and $2.8 \times 10^{-8}$ m$^2$ for the #36 Grit, #80 Grit, and #120 Grit fractures, respectively.

In the decreasing permeability stage, the permeability values decrease sharply as the shear displacements and shear stresses increase. This may be caused by the destruction of surface roughness, grain size reductions, and the rotation of crushed grains. These decreasing permeability values are consistent with the fault gouge–grain size relationship reported by Morrow et al. [41]. The results from the experiments run for this study show that a rougher fracture surface has a higher initial permeability and a larger permeability reduction after shearing than a smoother fracture surface. This result is analogous to the behavior reported for coarse-grained and fine-grained fault gouges. In addition, the rates at which the permeability is reduced in the permeability-decreasing stages are roughness dependent in that the permeability values along the rougher surfaces decrease more quickly than does the permeability for the sample with a smoother surface. This is because a rougher surface is flattened more quickly during shearing.

In the second stable stages, the permeability values oscillate. In the later stages of the experiments, the rock specimen's fracture surfaces are smoother and this results in fewer perturbations in the permeability versus shear-displacement curves. This change in permeability behavior is consistent with less stick-slip on the fracture surfaces.

Figure 5 shows the initial and final permeability values before and after the shearing tests for the three fractures. The changes in permeability decrease with decreasing fracture roughness. For most fractures, a rougher surface results in a higher porosity. During shearing, the rough fracture walls are smoothed and crushed grains can easily fill the fracture. With further shearing, the size of the crushed grains may be reduced further.

*4.2. Evolution of Shear-Induced Surface Roughness.* Photographs of the unsheared and sheared fracture surfaces are

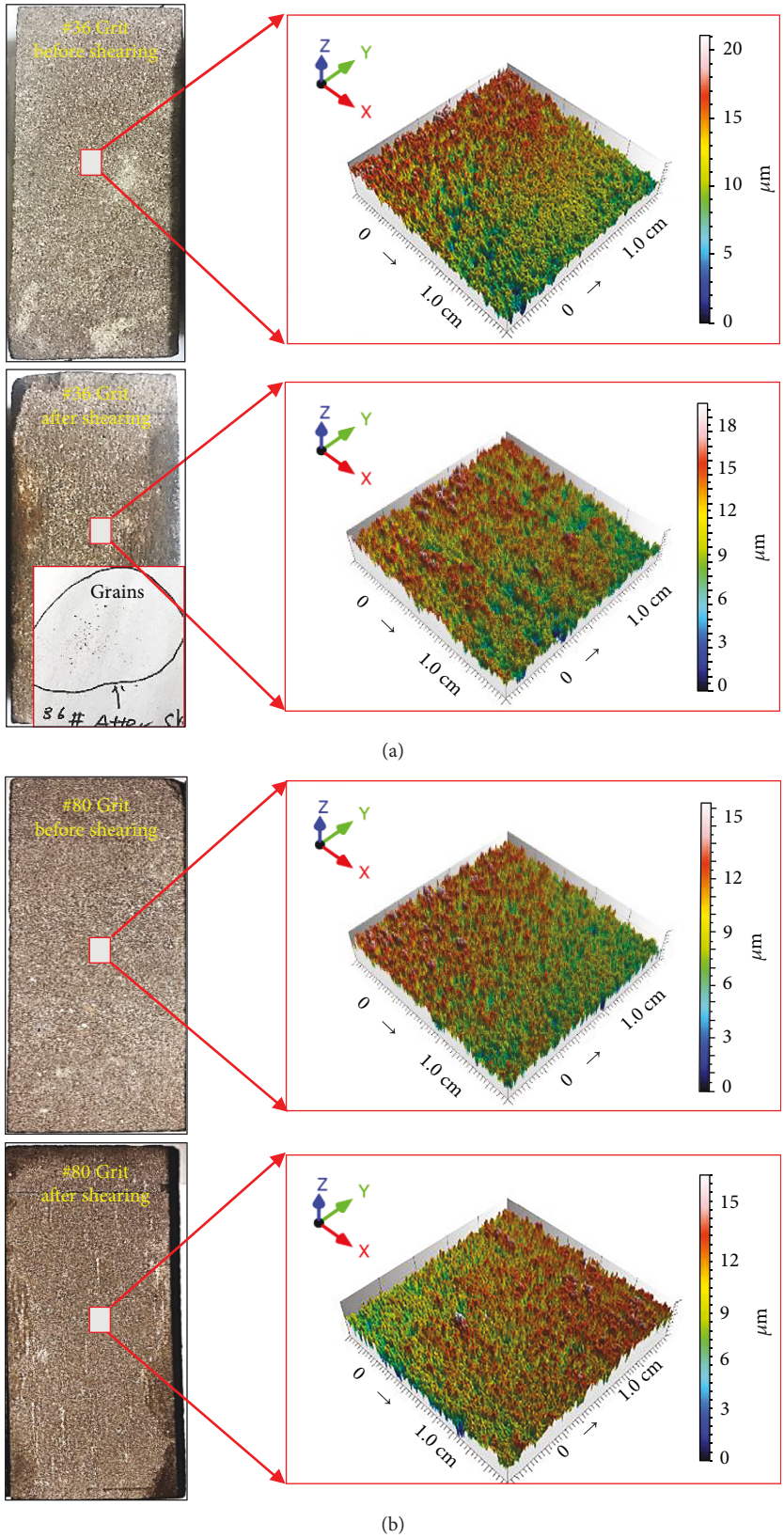


Figure 6: Continued.

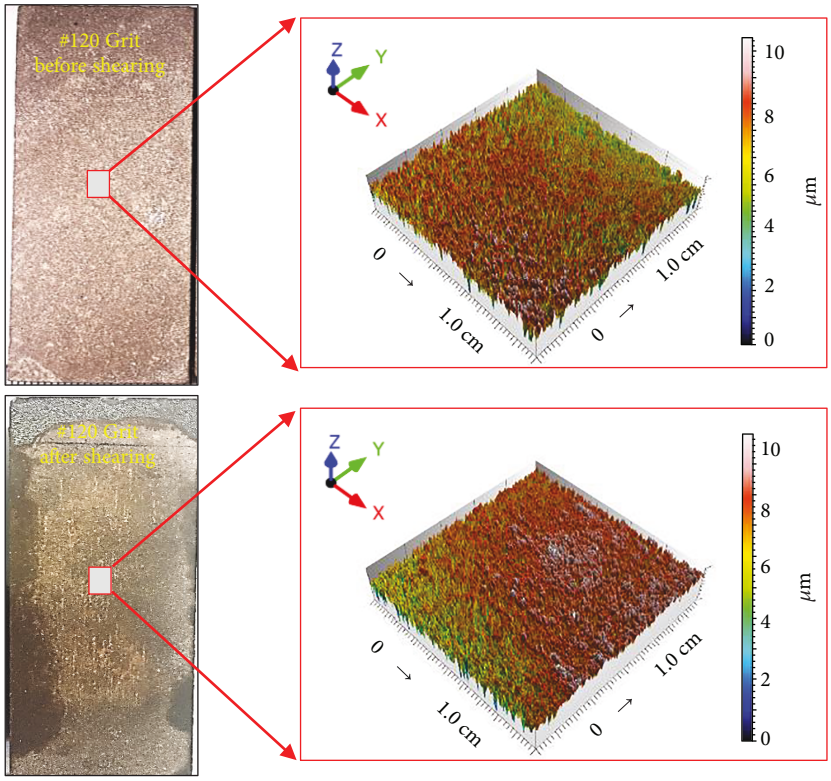


(c)

Figure 6: Unsheared and sheared fracture surfaces and the corresponding 3-D views: (a) #36 Grit; (b) #80 Grit; (c) #120 Grit.

presented in Figure 6 along with 3-D profilometer images of 10 mm × 10 mm areas near the center of each fracture. The upper and lower photographs in Figures 6(a)–6(c) show the unsheared and sheared fracture surfaces for each specimen, and the corresponding 3-D profilometer scans are on the right.

During shearing, the rough fracture surfaces were ground down and the coarse grains on the rough surfaces were crushed into fine powder. This resulted in a significant reduction in fracture aperture and permeability. This permeability decrease may be linked directly to the microstructural evolution of the flow pathways [23], which occurs via a complex interplay between matrix compaction and cataclastic fracture sealing. In addition, the gouge/wear effect is unavoidable during frictional sliding [32]. During sliding, gouge is produced and the presence of the gouge causes a further decrease in fracture permeability.

As mentioned above, 3-D views of portions of the fracture surfaces are shown on the right side of Figure 6. As can be seen from the photographs and 3-D images, the sheared surfaces are all scraped and the rougher the unsheared surface is, the more it has been scraped. Greater scraping may enhance permeability to some extent, but this scraping is dominated by abrasion. Intuitively, one might think that the surfaces would become rougher after being scraped, but the results suggest that this is not the case.

The test parameters were derived from the 3-D scanning results. Figure 7 shows the effect of shearing on the arithmetic mean height (Sa), root mean square height (Sq), maximum pit height (Sv), and maximum peak height (Sp) values. These parameters can be expressed as

$$\begin{aligned} \mathrm{Sa} &= \frac{1}{A}\iint |Z(x,y)|\,\mathrm{d}x\,\mathrm{d}y, \\ \mathrm{Sq} &= \sqrt{\frac{1}{A}\iint Z^2(x,y)\,\mathrm{d}x\,\mathrm{d}y}, \\ \mathrm{Sz} &= \mathrm{Sp} + \mathrm{Sv}, \\ \mathrm{Sp} &= \max\ Z(x,y), \end{aligned} \tag{4}$$

where $Z(x, y)$ is the height of the surface point under the corresponding $x$-location and $y$-location. $A$ is the scanning area of the sample surface.

In Figure 7, the black data points correspond to the parameters before shearing and the red data points mark the parameters after shearing. All of the parameters decrease with decreasing roughness, and most of them also decrease after shearing. However, as can be seen in Figures 7(a) and 7(b), the Sa and Sq values for the #36 Grit fracture surface are nearly the same or slightly greater after shearing. This may be due to scraping because, as mentioned, scraping can conceivably lead to an increase in permeability. The changes in permeability are caused not only by roughness reduction and scraping but also by the gouge being sealed by clay minerals or crushed grains. Therefore, it can be concluded that

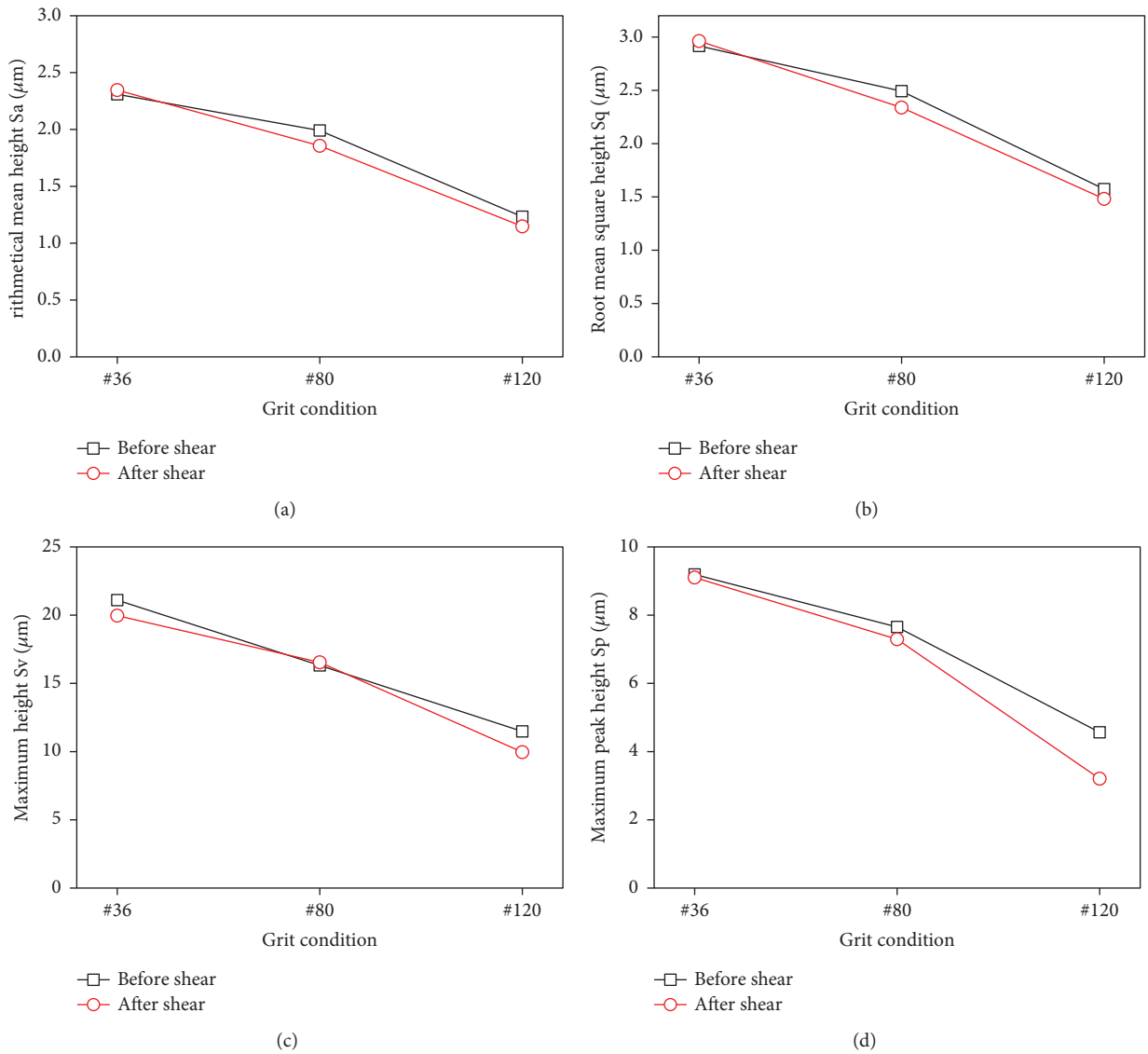


Figure 7: Surface parameters of unsheared and sheared sandstone fractures: (a) arithmetical mean height Sa; (b) root mean square height Sq; (c) maximum pit height Sv; (d) maximum peak height Sp.

the coupled grinding (plus scraping) and sealing effects could be the fundamental mechanism leading to decreased permeability in sheared sandstone fractures.

## 5. Conclusions

To understand the evolution of shear-induced permeability in saw-cut sandstone fractures with different types of roughness, we have presented the results from a suite of three experiments. These results allowed the mechanics of shear-permeability evolution to be deliberated, and several conclusions have been drawn:

(1) The shear stress-displacement curves for the saw-cut fractures can be divided into three stages: a stress adjustment stage, a stage of increasing stress, and a stable shear stage. Similarly, the corresponding permeability-displacement curves can also be divided into three stages, namely, a stable stage, a stage of decreasing permeability, and a second stable stage

(2) A rougher fracture surface undergoes greater damage during shearing. The greater the initial surface roughness, the greater the permeability drop after shearing

(3) The coupled effects of grinding (plus scraping) and sealing lead to a decrease in permeability. During shearing, fracture walls grind and scrape against each other, and this results in partial flattening of the fracture surface and the production of fault gouge in the fracture. In turn, this leads to flow pathways being blocked by crushed mineral grains

## Data Availability

The data used to support the findings of this study are available from the corresponding author upon request.

## Conflicts of Interest

The authors declare that there is no conflict of interest regarding the publication of this paper.

## Acknowledgments

The authors would like to express their sincere appreciation to Dr. Yi Fang (The University of Texas at Austin) for his contribution in this study. This work was supported by the Fundamental Research Funds for the Central Universities (2017XKZD06).

## References

[1] J. M. Kim, R. R. Parizek, and D. Elsworth, "Evaluation of fully-coupled strata deformation and groundwater flow in response to longwall mining," *International Journal of Rock Mechanics and Mining Sciences*, vol. 34, no. 8, pp. 1187–1199, 1997.

[2] H. Li and K. Fu, "Some major technical problems and countermeasures for deep mining," *Journal of Mining and Safety Engineering*, vol. 23, pp. 468–471, 2006.

[3] H. Gui and M. Lin, "Types of water hazards in China coalmines and regional characteristics," *Natural Hazards*, vol. 84, no. 2, pp. 1501–1512, 2016.

[4] W. X. Wang, W. H. Sui, B. Faybishenko, and W. T. Stringfellow, "Permeability variations within mining-induced fractured rock mass and its influence on groundwater inrush," *Environmental Earth Sciences*, vol. 75, no. 4, 2016.

[5] A. Kamali and A. Ghassemi, "In analysis of natural fracture shear slip and propagation in response to injection," in *41st Stanford Geothermal Workshop, Stanford University, Stanford, California*pp. 22–24, Stanford, California, 2016.

[6] P. Segall, "Earthquakes triggered by fluid extraction," *Geology*, vol. 17, no. 10, pp. 942–946, 1989.

[7] M. A. Antonellini and A. Aydin, "Effect of faulting on fluid flow in porous sandstones: petro-physical properties," *AAPG Bulletin*, vol. 78, pp. 355–377, 1994.

[8] M. A. Antonellini, A. Aydin, and D. D. Pollard, "Microstructure of deformation bands in porous sandstones at arches national park, Utah," *Journal of Structural Geology*, vol. 16, no. 7, pp. 941–959, 1994.

[9] Q. J. Fisher, J. Haneef, C. A. Grattoni, S. Allshorn, and P. Lorinczi, "Permeability of fault rocks in siliciclastic reservoirs: recent advances," *Marine and Petroleum Geology*, vol. 91, pp. 29–42, 2018.

[10] Q. J. Fisher and R. J. Knipe, "Fault sealing processes in siliciclastic sediments," *Geological Society London Special Publications*, vol. 147, no. 1, pp. 117–134, 1998.

[11] Q. J. Fisher and R. J. Knipe, "The permeability of faults within siliciclastic petroleum reservoirs of the North Sea and Norwegian continental shelf," *Marine and Petroleum Geology*, vol. 18, no. 10, pp. 1063–1081, 2001.

[12] Z. Feng, Y. Zhao, A. Zhou, and N. Zhang, "Development program of hot dry rock geothermal resource in the Yangbajing basin of China," *Renewable Energy*, vol. 39, no. 1, pp. 490–495, 2012.

[13] R. I. Borja and A. Aydin, "Computational modeling of deformation bands in granular media. I. Geological and mathematical framework," *Computer Methods in Applied Mechanics and Engineering*, vol. 193, no. 27-29, pp. 2667–2698, 2004.

[14] J. S. Caine, J. P. Evans, and C. B. Forster, "Fault zone architecture and permeability structure," *Geology*, vol. 24, no. 11, pp. 1025–1028, 1996.

[15] H. Yasuhara, D. Elsworth, and A. Polak, "Evolution of permeability in a natural fracture: significant role of pressure solution," *Journal of Geophysical Research Solid Earth*, vol. 109, no. B3, 2004.

[16] H. A. Sheldon, B. Florio, M. G. Trefry, L. B. Reid, L. P. Ricard, and K. A. R. Ghori, "The potential for convection and implications for geothermal energy in the Perth basin, Western Australia," *Hydrogeology Journal*, vol. 20, no. 7, pp. 1251–1268, 2012.

[17] F. Wang, C. Zhang, and N. Liang, "Gas permeability evolution mechanism and comprehensive gas drainage technology for thin coal seam mining," *Energies*, vol. 10, no. 9, p. 1382, 2017.

[18] W. Wu, Y. Gensterblum, J. S. Reece, and M. D. Zoback, "In Permeability Evolution with Shearing of Simulated Faults in Unconventional Shale Reservoirs," in *American Geophysical Union, Fall Meeting 2016*, San Francisco, CA, USA, 2016.

[19] G. Si, S. Jamnikar, J. Lazar et al., "Monitoring and modelling of gas dynamics in multi-level longwall top coal caving of ultra-thick coal seams, part i: borehole measurements and a conceptual model for gas emission zones," *International Journal of Coal Geology*, vol. 144-145, pp. 98–110, 2015.

[20] G. Si, J. Q. Shi, S. Durucan et al., "Monitoring and modelling of gas dynamics in multi-level longwall top coal caving of ultra-thick coal seams, part ii: numerical modelling," *International Journal of Coal Geology*, vol. 144-145, pp. 58–70, 2015.

[21] Y. Zhao, Z. Feng, Z. Feng, D. Yang, and W. Liang, "Thm (thermo-hydro-mechanical) coupled mathematical model of fractured media and numerical simulation of a 3d enhanced geothermal system at 573 K and buried depth 6000–7000 M," *Energy*, vol. 82, pp. 193–205, 2015.

[22] W. Wang, H. Wang, H. Li, D. Li, H. Li, and Z. Li, "Experimental enrichment of low-concentration ventilation air methane in free diffusion conditions," *Energies*, vol. 11, no. 2, p. 428, 2018.

[23] B. T. Ngwenya, O. Kwon, S. C. Elphick, and I. G. Main, "Permeability evolution during progressive development of deformation bands in porous sandstones," *Journal of Geophysical Research Solid Earth*, vol. 108, no. B7, 2003.

[24] K. B. Min, J. Rutqvist, C. F. Tsang, and L. Jing, "Stress-dependent permeability of fractured rock masses: a numerical study," *International Journal of Rock Mechanics and Mining Sciences*, vol. 41, no. 7, pp. 1191–1210, 2004.

[25] V. Vajdova, P. Baud, and T. F. Wong, "Permeability evolution during localized deformation in Bentheim sandstone," *Journal of Geophysical Research Solid Earth*, vol. 109, no. B10, 2004.

[26] A. Kotousov, L. Bortolan Neto, and S. S. Rahman, "Theoretical model for roughness induced opening of cracks subjected to compression and shear loading," *International Journal of Fracture*, vol. 172, no. 1, pp. 9–18, 2011.

[27] R. Olsson and N. Barton, "An improved model for hydromechanical coupling during shearing of rock joints," *International Journal of Rock Mechanics and Mining Sciences*, vol. 38, no. 3, pp. 317–329, 2001.

[28] I. W. Yeo, M. H. de Freitas, and R. W. Zimmerman, "Effect of shear displacement on the aperture and permeability of a rock fracture," *International Journal of Rock Mechanics and Mining Sciences*, vol. 35, no. 8, pp. 1051–1070, 1998.

[29] F. Lanaro, "A random field model for surface roughness and aperture of rock fractures," *International Journal of Rock Mechanics and Mining Sciences*, vol. 37, no. 8, pp. 1195–1210, 2000.

[30] C. A. Barton, M. D. Zoback, and D. Moos, "Fluid flow along potentially active faults in crystalline rock," *Geology*, vol. 23, no. 8, pp. 683–686, 1995.

[31] T. Tamagawa and D. D. Pollard, "Fracture permeability created by perturbed stress fields around active faults in a fractured basement reservoir," *AAPG Bulletin*, vol. 92, no. 6, pp. 743–764, 2008.

[32] C. H. Scholz, "Wear and gouge formation in brittle faulting," *Geology*, vol. 15, no. 6, pp. 493–495, 1987.

[33] Y. Kitagawa, K. Fujimori, and N. Koizumi, "Temporal change in permeability of the Nojima fault zone by repeated water injection experiments," *Tectonophysics*, vol. 443, no. 3-4, pp. 183–192, 2007.

[34] Y. Fang, D. Elsworth, C. Wang, T. Ishibashi, and J. P. Fitts, "Frictional stability-permeability relationships for fractures in shales," *Journal of Geophysical Research Solid Earth*, vol. 122, no. 3, pp. 1760–1776, 2017.

[35] I. Faoro, A. Niemeijer, C. Marone, and D. Elsworth, "Influence of shear and deviatoric stress on the evolution of permeability in fractured rock," *Journal of Geophysical Research Solid Earth*, vol. 114, no. B1, 2009.

[36] A. Ruina, "Slip instability and state variable friction laws," *Journal of Geophysical Research Solid Earth*, vol. 88, no. B12, pp. 10359–10370, 1983.

[37] J. YJ, W. A. Gang, and L. I. Bo, "Experimental study and analysis of shear-flow coupling behaviors of rock joints," *Chinese Journal of Rock Mechanics and Engineering*, vol. 26, pp. 2253–2259, 2007.

[38] W. Zhu and T. F. Wong, "The transition from brittle faulting to cataclastic flow: permeability evolution," *Journal of Geophysical Research*, vol. 102, no. B2, pp. 3027–3041, 1997.

[39] H. A. Sheldon and A. Ord, "Evolution of porosity, permeability and fluid pressure in dilatant faults post-failure: implications for fluid flow and mineralization," *Geofluids*, vol. 5, no. 4, 288 pages, 2005.

[40] W. Wu, J. S. Reece, Y. Gensterblum, and M. D. Zoback, "Permeability evolution of slowly slipping faults in shale reservoirs," *Geophysical Research Letters*, vol. 44, no. 22, pp. 11368–11375, 2017.

[41] C. A. Morrow, L. Q. Shi, and J. D. Byerlee, "Permeability of fault gouge under confining pressure and shear stress," *Journal of Geophysical Research Solid Earth*, vol. 89, no. B5, pp. 3193–3200, 1984.

[42] Y. Kitagawa, K. Fujimori, and N. Koizumi, "Temporal change in permeability of the rock estimated from repeated water injection experiments near the Nojima fault in Awaji island, Japan," *Geophysical Research Letters*, vol. 29, no. 10, pp. 121-1–121-4, 2002.

[43] H. A. Sheldon and S. Micklethwaite, "Damage and permeability around faults: implications for mineralization," *Geology*, vol. 35, no. 10, pp. 903–906, 2007.

[44] ISO. Iso 25178-2, *Geometrical Product Specifications (GPS) - Surface Texture: Areal Part 2: Terms, Definitions and Surface Texture Parameters*, International Organization for Standardization, 2012.

[45] J. Bear, C. F. Tsang, and G. D. Marsily, *Flow and Contaminant Transport in Fractured Rock*, Elsevier, 1993.

[46] D. L. Hopkins, "The implications of joint deformation in analyzing the properties and behavior of fractured rock masses, underground excavations, and faults," *International Journal of Rock Mechanics and Mining Sciences*, vol. 37, no. 1-2, pp. 175–202, 2000.

[47] A. Niemeijer, C. Marone, and D. Elsworth, "Frictional strength and strain weakening in simulated fault gouge: competition between geometrical weakening and chemical strengthening," *Journal of Geophysical Research Solid Earth*, vol. 115, no. B10, 2010.